



Article

Magnetomechanical Stress-Induced Colon Cancer Cell Growth Inhibition

Katerina Spyridopoulou ¹, Georgios Aindelis ¹, Charalampos Sarafidis ², Orestis Kalogirou ² and Katerina Chlichlia ^{1,*}

¹ Department of Molecular Biology and Genetics, University Campus Dragana, Democritus University of Thrace, 68100 Alexandroupolis, Greece

² Department of Physics, Aristotle University of Thessaloniki, 54124 Thessaloniki, Greece

* Correspondence: achlichl@mbg.duth.gr; Tel.: +30-25510-30630

Abstract: The application of magnetomechanical stress in cells using internalized magnetic nanoparticles (MNPs) actuated by low-frequency magnetic fields has been attracting considerable interest in the field of cancer research. Recent developments prove that magnetomechanical stress can inhibit cancer cells' growth. However, the MNPs' type and the magnetic field's characteristics are crucial parameters. Their variability allows multiple combinations, which induce specific biological effects. We previously reported the antiproliferative effects induced in HT29 colon cancer cells by static-magnetic-field (200 mT)-actuated spherical MNPs (100 nm). Herein, we show that similar growth inhibitory effects are induced in other colon cancer cell lines. The effect of magnetomechanical stress was also examined in the growth rate of tumor spheroids. Moreover, we examined the biological mechanisms involved in the observed cell growth inhibition. Under the experimental conditions employed, no cell death was detected by PI (propidium iodide) staining analysis. Flow cytometry and Western blotting revealed that G2/M cell cycle arrest might mediate the antiproliferative effects. Furthermore, MNPs were found to locate in the lysosomes, and a decreased number of lysosomes was detected in cells that had undergone magnetomechanical stress, implying that the mechanical activation of the internalized MNPs could induce lysosome membrane disruption. Of note, the lysosomal acidic conditions were proven to affect the MNPs' magnetic properties, evidenced by vibrating sample magnetometry (VSM) analysis. Further research on the combination of the described magnetomechanical stress with lysosome-targeting chemotherapeutic drugs could lay the groundwork for the development of novel anticancer combination treatment schemes.

Keywords: magneto-mechanical stress; MNPs; colon cancer; growth inhibition; cell cycle arrest; lysosomes



Citation: Spyridopoulou, K.; Aindelis, G.; Sarafidis, C.; Kalogirou, O.; Chlichlia, K. Magnetomechanical Stress-Induced Colon Cancer Cell Growth Inhibition. *J. Nanotheranostics* **2022**, *3*, 134–150. <https://doi.org/10.3390/jnt3030010>

Academic Editor: Moein Moghimi

Received: 16 July 2022

Accepted: 22 August 2022

Published: 26 August 2022

Publisher's Note: MDPI stays neutral with regard to jurisdictional claims in published maps and institutional affiliations.



Copyright: © 2022 by the authors. Licensee MDPI, Basel, Switzerland. This article is an open access article distributed under the terms and conditions of the Creative Commons Attribution (CC BY) license (<https://creativecommons.org/licenses/by/4.0/>).

1. Introduction

Mechanical stimulation is a very promising strategy, based on which novel therapeutic biomedical technologies can be developed. Mechanical stimulation is known to affect the growth and differentiation of stem cells [1], and thus, various applications employing this strategy have been proposed in the fields of tissue engineering and regenerative medicine [2]. Interestingly, mechanoresponsive genes have been identified, highlighting that mechanical stress alone can regulate the transcription of certain genes [3]. Mechanical forces are considered to be significant regulators in tumor growth, metastasis, as well as anticancer treatment response [4]. In fact, various studies have described the inhibition of tumor growth in preclinical tumor models, which is achieved solely by mechanical effects [5–7]. Interestingly, various oncogenes have been found to activate the same signaling processes that are triggered as a response to mechanical stress [8].

The effects of mechanical forces applied on cells are dependent on the forces' characteristics such as the direction, magnitude, and duration of the force application [9]. Therefore,

it is significant to apply specific forces on cells, with great precision and accuracy. The ability to apply these precisely controllable forces could be a critical tool for the development of innovative and efficient anticancer biomedical strategies.

However, precision at the cellular scale is quite difficult to achieve. Magnetic nanoparticles, being structures whose dimensions lie in the nanoscale, constitute an excellent tool for such meticulously defined precision. Moreover, their magnetic properties allow for the remote, controlled, and non-invasive application of the defined mechanical forces at the magnitude, direction, and application time required [10,11].

Examples of biomedical applications of externally controlled MNPs are the achievement of magnetically driven endocytosis in prostate cancer PC-3 cells [12], magnetic cell levitation [13], and the induction of swelling and apoptosis in THP-1 monocytic leukemia cells [14]. It is becoming evident that MNPs, allowing for the highly controllable application of magnetomechanical forces when being exposed to tunable magnetic fields, offer various possibilities as a stimuli-responsive system, which can be employed in novel biomedical applications.

Alternating magnetic fields specifically have been employed in various studies in order to remotely control MNPs for the intracellular triggering of cellular responses. Endocytosed MNPs, actuated by an external alternating magnetic field, have been shown to destabilize the membrane of lysosomes through mechanical disruption, which leads to cell death due to the release of the highly acidic lysosomal contents into the cytoplasm [15,16]. Moreover, MNPs may specifically bind to the cancer cell membrane and induce cell death by exerting magnetomechanical stress [17,18]. Importantly, the intracellular localization of the mechanical-force-applying MNPs has been proven to be more efficient in damaging cancer cells than the membrane-bound localization [18].

Therefore, applying localized mechanical stress appears to be a very promising tool in cancer research, as it can have a profound effect on cancer cell proliferation and tumor growth kinetics [19]. In this context, various magnetic nanostructures have been investigated as potential tools for the application of magnetomechanical stress under magnetic field exposure in cancer cells [20]. Kim et al. used magnetic disk-shaped structures to mechanically disrupt the membrane of cancer cells, resulting in a 90% inhibition in cell growth [21], while Shen et al. used MNPs' elongated aggregates to induce necrosis in cancer cells by disrupting both the lysosomal and the cellular membranes [22]. Magnetic nanocubes were employed for targeting mitochondria and inducing apoptosis via mechanical stress *in vitro* and *in vivo* in preclinical glioblastoma models [23]. Furthermore, magnetomechanical stress applied through actuated magnetic nanowires was described to enhance the doxorubicin anticancer effect *in vitro* [24]. Cylindrical magnetic nanoparticles have also been used for inducing apoptosis in cancer cells via magnetomechanical stress effects [25]. Besides the variety of structures with shape anisotropy available, among the most commonly used types of nanoparticles for the application of magnetomechanical stress in cancer cells are spherical nanoparticles [20].

Our team previously comparatively examined the antiproliferative effects of spherical magnetite MNPs with a hydrodynamic diameter of 100 nm actuated by static or alternating low-frequency magnetic fields with varying intensity (40–200 mT), frequency (0–8 Hz), and field gradients in HT29 colon cancer cells. We reported that the highest inhibition of cell growth (47% of control cell growth) was generated by the static field of the strongest field intensity (200 mT) and gradient [26]. This correlation between field intensity and the growth inhibitory effect is extremely interesting, and in this line, we proceeded to investigate herein the biological mechanisms involved.

Therefore, in this study, we examined whether the previously observed antiproliferative effects induced by magnetomechanical stress, applied via static-magnetic-field (200 mT)-actuated MNPs in HT29 colon cancer cells, is also induced in other colon cancer cell lines. Next, we investigated whether the induced cell growth inhibition is mediated by cell death and/or cell cycle arrest. Furthermore, we examined the effects of magnetic-field-exposed MNPs in HT29 3D tumor spheroids and investigated the intracellular localization

of the endocytosed nanoparticles, which were found to accumulate in lysosomes. Consecutively, we examined lysosomes' integrity after the exposure of their MNP content to the magnetic field and its effect on the cell growth rate. We believe that future applications of our findings could lead to the development of anticancer combination treatment schemes that are based on these MNPs, utilizing their lysosome-targeting properties and/or combining the cytostatic effect induced by field exposure in MNP-treated cells, with standard chemotherapeutic drugs, achieving enhanced anticancer potential.

2. Materials and Methods

2.1. Materials

Dulbecco's Modified Eagle's Medium (DMEM) was purchased from Gibco (Waltham, MA, USA). Fetal bovine serum (FBS), trypsin, penicillin/streptomycin, and phosphate-buffered saline (PBS) were purchased from Biosera (Boussens, France). Hoechst 33342, LysoTracker Red, and LysoTracker Blue were purchased from Invitrogen (ThermoFischer, Waltham, MA, USA). Propidium iodide (PI), RNase A, acetic acid, trichloroacetic acid (TCA), Trizma base, sulforhodamine B (SRB), and all other chemicals mentioned were purchased from Sigma-Aldrich (St. Louis, MO, USA).

2.2. Cell Lines

Colon carcinoma cell lines were obtained from ATCC. Cells of mouse (CT26) or human (HT29 and Caco-2) origin were maintained in a humidified incubator with 5% CO₂ at 37 °C. Cells were grown in DMEM supplemented with 10% FBS, 100 U/mL penicillin, 100 µg/mL streptomycin, and 2 mM glutamine.

2.3. MNPs Treatment and Magnetic Field Exposure

Cells were handled as described in Spyridopoulou et al. [26]. Briefly, cells were seeded in 35 mm cell culture dishes, left to adhere overnight, and treated with 100 µg/mL MNPs (fluidMAG-D, Chemicell, GmbH, Berlin, Germany) for the indicated time points. For the fluorescence microscopy and the fluorescence flow cytometry experiments, fluorescently labeled nanoparticles (fMNPs) with the same properties were used (nano-screenMAG/R-D). The MNPs used are aqueous dispersions of magnetic iron oxides with an average hydrodynamic diameter of 100 nm, coated with starch. After incubation with the MNPs, cells were thoroughly washed with PBS to remove the MNPs that had not been internalized. Fresh culture medium was added, and the cells were exposed for 30 min to the static magnetic field of 200 mT generated by a Nd-Fe-B block magnet, as previously described. The magnetic field was calculated with COMSOL Multiphysics 3.5a (COMSOL Inc., Stockholm, Sweden), and the calculations were validated by measurements performed with a Hall Probe (THM 1176-MF, MetroLab Technology, Plan-les-Ouates, Switzerland). For a detailed characterization of the magnetic field, see Spyridopoulou, K. et al. (2018) and Maniotis, N. et al. (2017) [26,27]. Finally, treated cells were handled according to the assay employed.

2.4. Cell Growth Assay

Cell growth was analyzed with the Sulforhodamine B (SRB) assay [28]. Cells were seeded in 96-well plates and left to adhere overnight. Then, cells were fixed with TCA, dried, and stained, as previously described [29]. Optical density was measured with a microplate reader (Enspire, Perkin Elmer, Waltham, MA, USA). Appropriate controls to exclude the background signal due to the presence of MNPs were included. The inhibition of the cell growth percentage was calculated by the following formula:

$$\% \text{ growth inhibition} = 100 - [(\text{mean OD sample})/(\text{mean OD control}) \times 100]$$

2.5. Fluorescence Microscopy

Samples were examined under a Zeiss Axio Scope A1 microscope (Zeiss Microscopy, Göttingen, Germany), and image acquisition was performed using the ZEN Blue imaging

software (Zeiss Microscopy, Göttingen, Germany). For fluorescence confocal microscopy, live cells were visualized by confocal fluorescence microscopy on 8-well chambered glass coverslips (μ -slides, IBIDI, Gräfelfing, Germany), and imaging was performed on a customized Andor Revolution Spinning Disc Confocal System built around a stand (IX81; Olympus, Tokyo, Japan) with a digital camera (Andor Nikon+885, Andor Technology, Oxford Instruments, Abingdon, United Kingdom) (CIBIT Facility, MBG-DUTH). Image acquisition was performed with the Andor IQ2 software (Andor Technology, Oxford Instruments, Abingdon, United Kingdom). Image analysis was performed with the ImageJ v.1.50i software (U. S. National Institutes of Health, Bethesda, MD, USA).

2.6. Assessment of Cell Death

Cell death was analyzed by PI staining. Upon treatment, cells were either harvested by trypsinization (for flow cytometry analysis) or moved by handling the coverslip on which they were grown with forceps in a new culture dish filled with PBS (for fluorescence microscopy). Cells on the coverslip were stained with Hoechst 33342 for 40 min at 37 °C and, subsequently, with PI. Cells in suspension intended for flow cytometry analysis were only stained with PI. Excess dye was washed away with PBS, and cells in suspension were analyzed on the flow cytometer (Attune NxT flow cytometer, Thermo Fisher Scientific, Waltham, MA, USA), while data analysis was performed with the FlowJo V10 software (FlowJo LCC, Ashland, OR, USA), then cells on the coverslip were observed under a fluorescence microscope as described in Section 2.5.

2.7. Assessment of the Structural Integrity of Lysosomes

Cells were either grown on coverslips (for fluorescence microscopy) or in 100 mm cell culture dishes (for flow cytometry). Two hours after the exposure of cells to the magnetic field, cells were incubated with LysoTracker Red (50 nM) for 30 min. Cells treated with +MNP-Field, -MNP-Field, and -MNP+Field were also assayed (+/- MNP indicates cells incubation or not, respectively, with 100 μ g/mL MNPs (fluidMAG-D or nano-screenMAG/R-D as stated) for 48 h unless a different time period is stated; +/- Field indicates whether cells have been exposed (+) or not (-) to the 200 mT static magnetic field for 30 min unless a different time point is mentioned). Coverslip-grown cells were visualized under a fluorescence microscope as described in Section 2.5. Images of multiple cells per treatment group were captured and analyzed with the ImageJ software, and the number of lysosomes was counted (as visible fluorescence spots). The results are expressed as % change compared to the number counted in -MNP-Field (control) cells. At least six cells per group were analyzed in three independent experiments. Cells grown in culture dishes were harvested by trypsinization, washed, resuspended in PBS, and analyzed on the flow cytometer (Attune NxT, Thermo Fisher Scientific, Waltham, MA, USA) for the detection of LysoTracker fluorescence intensity. Data analysis was performed with the FlowJo V10 software (FlowJo LCC, Ashland, OR, USA).

2.8. Co-Localization of the MNPs with the Lysosomes

After the incubation of the cells grown in μ -slides with fMNPs for the indicated time points (30 min, 12 h, 24 h, or 48 h), cells were incubated with LysoTracker Blue (50 nM) for 30 min, before visualization under the confocal microscope, as described in Section 2.5. At least eight cells from each time point group were analyzed in three independent experiments.

2.9. Cell Cycle Analysis

The cell cycle was analyzed by DNA content quantification with PI staining. Cells were synchronized and incubated in serum-free medium for 24 h prior to treatment. Treated cells were harvested by trypsinization, washed out with PBS, and fixed and permeabilized in 70% ice-cold ethanol. Fixed cells were incubated at -20 °C for at least 24 h prior to analysis. On the day of the analysis, the ethanol was washed and cells were incubated

with RNase A (10 µg/mL) and PI (50 µg/mL) for 40 min at room temperature in the dark. The cell cycle distribution was then analyzed on the flow cytometer. Data analysis was performed with the FlowJo V10 software (FlowJo LCC, Ashland, OR, USA).

2.10. Cyclin D1 and Cyclin B1 Protein Expression

Expression levels of cyclins D1 and B1 were analyzed by Western blot. Treated cells were lysed in RIPA buffer supplemented with protease inhibitors (100 µg/mL phenylmethylsulfonylfluoride (PMSF), 0.5 µg/mL leupeptin, 1.0 µg/mL pepstatin A, and 0.5 µg/mL aprotinin). The BCA protein assay was employed to determine the protein concentration in cell samples. The Pierce BCA protein assay kit was used according to the manufacturer's protocol. Sixty micrograms of protein extracts was loaded in a 10% SDS-polyacrylamide gel, and following electrophoresis, proteins were blotted on 0.45 µm PVDF membranes. Membranes were blocked with 5% *w/v* BSA/TBST solution and incubated overnight, at 4 °C with primary antibodies against cyclin B1 (1:1000, 4138 Cell Signaling, Danvers, MA, USA) or cyclin D1 (1:500, 2978 Cell Signaling) in 5% *w/v* BSA/TBST. Following overnight incubation, membranes were washed with TBST and incubated with HRP-conjugated anti-rabbit secondary antibody (1:5000). Protein bands were visualized using the ECL/HRP chemiluminescent substrate and autoradiography film. Membranes were stripped with a stripping buffer (15 g/L glycine, 1 g/L SDS, 10 mL/L Tween20, pH 2.2) and incubated with anti-β-tubulin antibody (1:20,000, T7816, Sigma Aldrich), in 5% *w/v* non-fat dry milk in TBST. A pre-stained protein ladder was used to monitor protein molecular weight (Nippon Genetics, Düren, Germany). Western blot densitometry band quantification was performed with ImageJ.

2.11. Tumor Spheroids

Tumor spheroids were generated according to the hanging drop method [30]. Briefly, cells pretreated with MNPs (100 µg/mL, 48 h) were subjected to the magnetic field and, after an overnight incubation, were harvested and resuspended in culture medium at a density of 12,500 cells per ml. The cell suspension was seeded in 20 µL drops inside an inverted 60 mm cell culture dish lid, which was filled with PBS to act as a hydration chamber. Ten drops were seeded per dish. The cells were left undisturbed for at least 24 h, following daily photographic observation under a bright field microscope (Zeiss PrimoVert Inverted Microscope equipped with a ZEISS Axiocam ERC 5C camera). The medium was replenished after 48 h. For the estimation of the spheroids' volume, images for analysis were captured at the indicated timepoints with the microscope's camera. Using ImageJ software, we determined the *width* and *length* of each spheroid. The volume of each spheroid was calculated with the modified ellipsoid formula:

$$V = \text{width}^2 \times \text{length} / 2$$

At least 10 spheroids were analyzed per group, and three independent experiments were performed.

2.12. Magnetic Characterization of the MNPs

In order to investigate whether the acidic lysosomal environment affects the magnetic properties of the MNPs, we examined their mass magnetization following treatment with an acidic (pH = 4.5) or a neutral solution (deionized water, DIW) for 24 h at 37 °C. For the acidic solution, a citrate buffer was prepared by mixing citric acid 0.1 M with trisodium citrate 0.1 M at 1/1.25 *v/v*. After the 24 h treatment, the MNPs were recovered by centrifugation (15,000 × *g*, 20 min) and three washes in DIW. The samples were freeze-dried (lyophilized) for 24 h in a BenchTop Pro (Virtis, SP Scientific, Warminster, PA, USA) dryer. The magnetic measurements were performed using a vibrating sample magnetometer (VSM) (Laboratory of Magnetism and Magnetic Materials, Department of Physics, Aristotle University of Thessaloniki, Greece). The oscillation frequency was 60 Hz, and the maximum applied field was 2 T.

2.13. Data Analysis and Statistics

All data are representative of at least three independent experiments unless stated otherwise, and the values are presented as the mean \pm S.D. All data were analyzed with Sigma Plot v. 11.0. or Excel v. 10. Statistical comparisons between groups were performed using Student's *t*-test. Differences between groups were considered statistically significant when $p < 0.05$ (* $p < 0.05$, ** $p < 0.01$, *** $p < 0.001$).

3. Results

Based on our previous results presented in Spyridopoulou et al. [26], we concluded that, among the static, rotating, and alternating magnetic field settings examined, it was the static magnetic field of the strongest intensity and gradient (200 mT) that induced the highest inhibition of cell growth in MNP-treated HT29 colon cancer cells. Therefore, in the present study, all field-treated cells were exposed to a static magnetic field of 200 mT for 30 min.

3.1. Effect of Magnetomechanical Stress on the Growth of Colon Cancer Cell Lines

First, we investigated whether the observed growth inhibitory effects of the 200 mT static magnetic field were also induced in other colon cancer cell lines besides HT29. Therefore, after confirming that 100 $\mu\text{g}/\text{mL}$ MNPs was not toxic to either CT26 or Caco-2 cells following a 48 h incubation period, we comparatively studied the effect of magnetic field exposure on the growth rate of the MNP-treated cells. Both CT26 and Caco-2 cells' proliferation rates were inhibited by the magnetic field, to a different degree. Specifically, a 55% or 70% inhibition in cell growth was observed for CT26 or Caco-2 cells, respectively (Figure 1A).

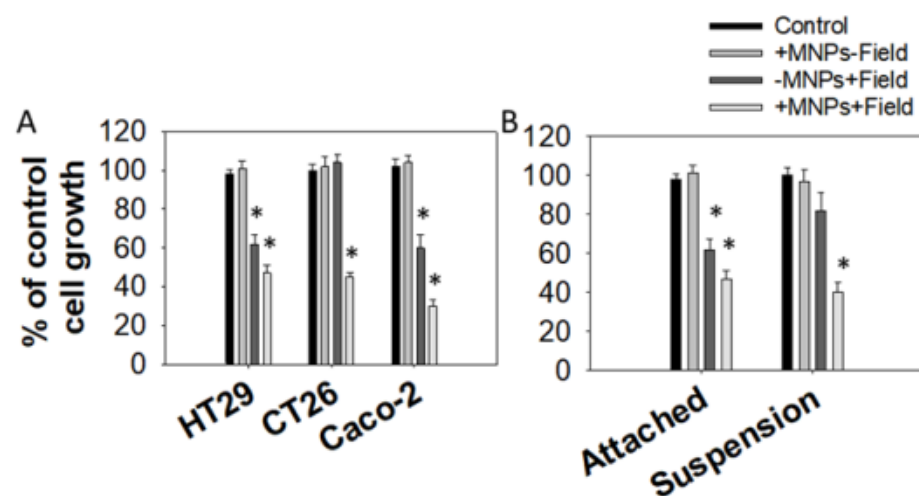


Figure 1. Effect of magnetomechanical treatment on the growth of colon cancer cells. (A) Comparison between different cell lines. (B) Comparison between attached and suspended HT29 cells. HT29, CT26, or Caco-2 cells were treated with 100 $\mu\text{g}/\text{mL}$ MNPs and/or exposed to a static magnetic field of 200 mT. Values represent the mean ($n = 3$) \pm S.D. * Asterisks indicate a statistically significant difference compared to the control (Student's *t*-test, $p \leq 0.05$).

Since the applied magnetomechanical force exerted by the magnetic-field-exposed internalized MNPs has a certain direction that depends on the direction of the applied magnetic field, we decided to investigate whether the geometry and relative orientation of the cell to the magnetic field affect the induced growth inhibitory effect. Both attached and suspended MNP-treated HT29 cells were similarly affected by magnetic field exposure as a growth rate of 47% or 40% was observed, respectively (Figure 1B). Noteworthy, the field's effect on cells that had not been treated with MNPs ($-$ MNPs+Field) was more profound in suspension as compared to attached cells (38% and 16% inhibition, respectively).

3.2. Cell Growth Inhibition Due to Magnetomechanical Stress Is Mediated by Cell Cycle Arrest

Despite the 40% or 47% cell growth inhibition observed for $-MNP+Field$ or $+MNP+Field$ cells, respectively (Figure 1A), neither $-MNP+Field$, nor $+MNP-Field$, nor $+MNP+Field$ cells exhibited a larger number of dead cells compared to control ($-MNP-Field$) cells, evidenced by the fluorescence microscopy of PI-stained cells (Figure 2A). This observation was further quantitatively confirmed with flow cytometric analysis (Figure 2B). In $+MNP+Field$ cells, only 13.5% of the cell population was dead, while, in the other groups, the percentages of dead cells were similarly low and no different from the control (7.6–13.9%). Two background controls that were not incubated with PI were also included in the analysis to assess the false positive signal MNPs might generate. As is depicted in Figure 2B, there was no MNP-derived background signal. We repeated the flow cytometry analysis of PI-stained cells immediately after the cellular exposure to the magnetic field (Figure 2B, 0 h) and 24 h later (Figure 2B, 24 h), and the results were similar to those collected for the cells that had been left to rest for 16 h after the field exposure (Figure 2B, 16 h). Taken together, these results suggest that the observed inhibition of cell growth in $+MNP-Field$ or $-MNP+Field$ cells cannot be attributed to cell death for the time period tested.

Having observed a 47% inhibition in proliferation, but no cell death in $+MNP+Field$ cells at the indicated time points, we proceeded to investigate whether the observed cell growth inhibition could be attributed to cell cycle arrest. Indeed, 24 h after exposure to the field, the percentage of cells in the G2/M phase was found to be higher in $+MNP+Field$ cells (37% of cell population in G2/M phase) compared to either $-MNP-Field$ (23% of cell population in G2/M phase), $+MNP-Field$ (25% of cell population in G2/M phase), or $-MNP+Field$ (28% of cell population in G2/M phase) cells (Figure 3A). Furthermore, we examined the protein expression of cyclins B1 and D1. Expression levels of cyclin B1, a master regulator of the G2/M transition, were upregulated 24 h post magnetic field exposure in $\pm MNP+Field$ cells (Figure 3B(i,ii)). Moreover, levels of cyclin D1, which are expected to be elevated in the G2 phase, were moderately enhanced in $+MNP\pm Field$ cells as compared to control $-MNP-Field$, 24 h after magnetic field exposure (Figure 3B(i,iii)).

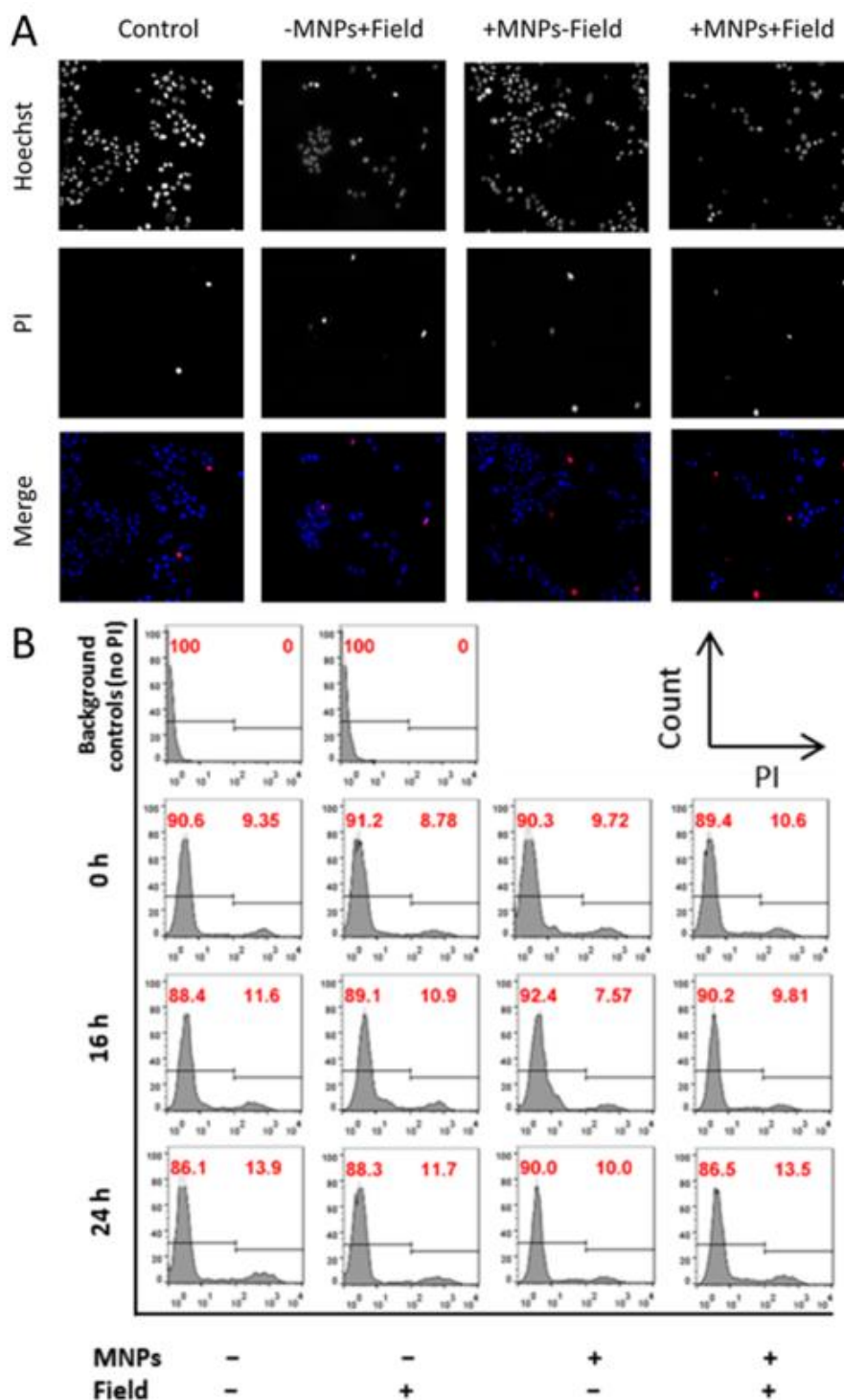


Figure 2. Propidium iodide live/dead cells analysis. (A) Fluorescence microscopy images of HT29 cells stained with the fluorescent DNA dyes Hoechst (blue) and PI (red). Nuclei of live cells appear blue, while nuclei of dead cells appear red. Cells were treated with MNPs (100 µg/mL, 48 h) and/or exposed to a static magnetic field of 200 mT and left undisturbed for 16 h before analysis. (B) Flow cytometry analysis of cell death. HT29 cells were treated with MNPs and/or exposed to a static magnetic field of 200 mT. The analysis of cell death was performed by PI exclusion. Cells were analyzed on a flow cytometer immediately (0 h), 16 h, or 24 h after the magnetic field exposure. Numbers in histograms indicate the percentage (%) of cells within each respective gate relative to the whole cell population. Results presented are representative of three independent experiments.

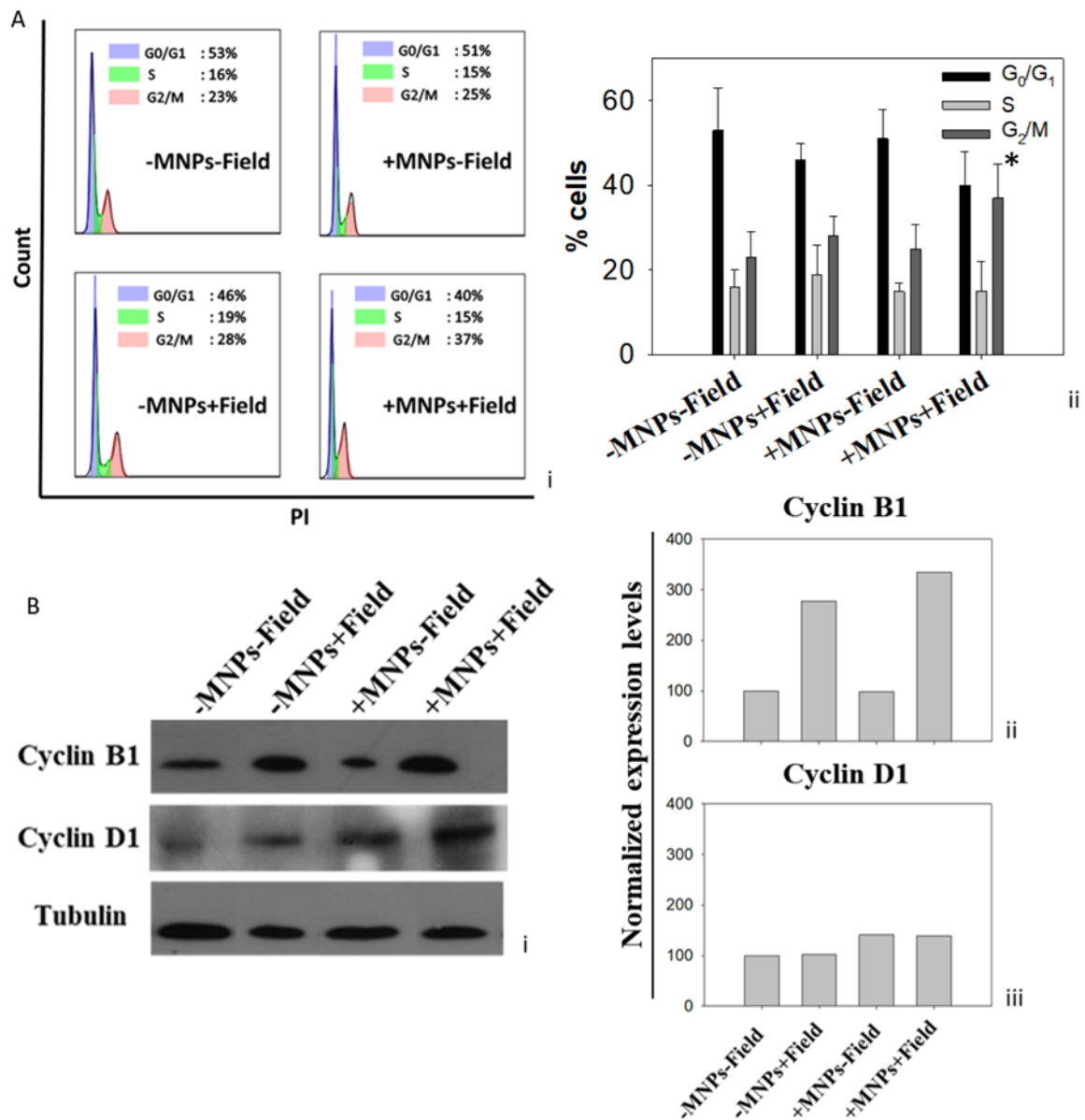


Figure 3. Effect of magnetic field exposure on cell cycle. **(A)** Cell cycle analysis after magnetic field exposure. HT29 cells were treated with MNPs, synchronized, and/or exposed to a static magnetic field of 200 mT. Flow cytometry analysis was performed 24 h post magnetic field exposure. **(Ai)** Flow cytometry histograms are representative of four independent experiments. **(Aii)** The data are presented as the means \pm SD of three independent experiments. * Asterisk indicates statistical significance compared to the control (–MNPs–Field) group, Student’s *t*-test, $p = 0.031$. **(B)** Expression of cyclin B1 and cyclin D1. **(Bi)** Western blot analysis of cyclin D1 and cyclin B1 expression levels in \pm MNPs \pm Field HT-29 cells. Cells were treated with MNPs and/or exposed to a static magnetic field of 200 mT. Cells were collected and lysed 24 h post magnetic field exposure. Densitometry analysis of the immunostaining results. Expression of cyclins **(Bii)** B1 and **(Biii)** D1 is presented as a normalized fold change compared to control (–MNPs–Field) expression levels (100%). Results presented are representative of two independent experiments. Tubulin was used as the normalization control.

3.3. Magnetomechanical Stress Effects on 3D Tumor Spheroids

The effect of magnetomechanical stress on cell growth was subsequently assessed in 3D tumor spheroids. Cells pretreated with MNPs (100 μ g/mL, 48 h) were subjected to the magnetic field and, after an overnight incubation, were seeded according to the

hanging drop method in order to form 3D tumor spheroids. After 96 h, the spheroids that had been formed out of the +MNP+Field cells were smaller compared to all the other groups. Specifically, the volume growth rate of spheroids between days 0 and 4 (96 h) for +MNP+Field cells was 60% relative to the growth rate exhibited by the control (−MNP−Field) ($n = 10$) (Figure 4).

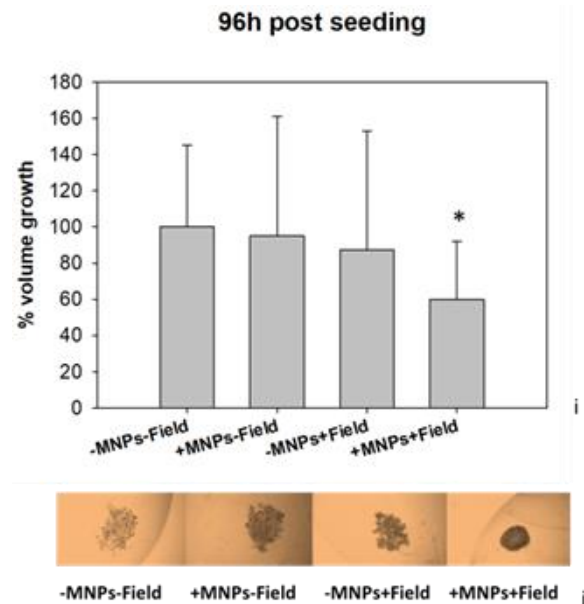


Figure 4. Effect of magnetomechanical stress on the growth of tumor spheroids. Percentage of volume growth is expressed relative to the growth of control cells (−MNP−Field) and refers to the difference in spheroids' volume between Day 0 and Day 4 post seeding. HT29 cells were seeded 24 h after the magnetic field exposure. (i) Spheroids' volume growth at 96 h post seeding expressed as % relative to control. Data presented as means ± SD. (ii) Photographs of representative spheroids captured at 96 h post seeding. At least 10 ($n = 10$) spheroids were analyzed. * Asterisk indicates a statistically significant difference (Student's t -test, $p \leq 0.05$).

3.4. MNPs Accumulate in the Lysosomes

Fluorescence microscopy showed that a proportion of the MNPs that the cells had uptaken accumulated in the lysosomes (Figure 5C,D). It is of interest that a greater degree of co-localization between lysosomes and MNPs occurred in shorter co-incubation periods (30 min–48 h) (Figure 5D). Next, we enquired whether the applied magnetomechanical stress in the lysosomes via actuated MNPs was strong enough to induce lysosomal membrane permeabilization (LMP), a phenomenon that could be involved in the growth inhibition observed. A smaller number of lysosomes was observed in +MNP+Field cells (72%) compared to control (−MNP−Field) cells (100%) (Figure 5A). Independent exposure to either MNPs (+MNP−Field) or Field (−MNP+Field) did not affect the number of lysosomes. Furthermore, the acidity of lysosomes (as an indicator of their structural integrity) was evaluated by flow cytometry with LysoTracker staining 2 h after magnetic field exposure. The fluorescence intensity of LysoTracker was attenuated in +MNP+Field cells (Figure 5B), indicating fewer lysosomes per cell and/or an increased pH in lysosomes.

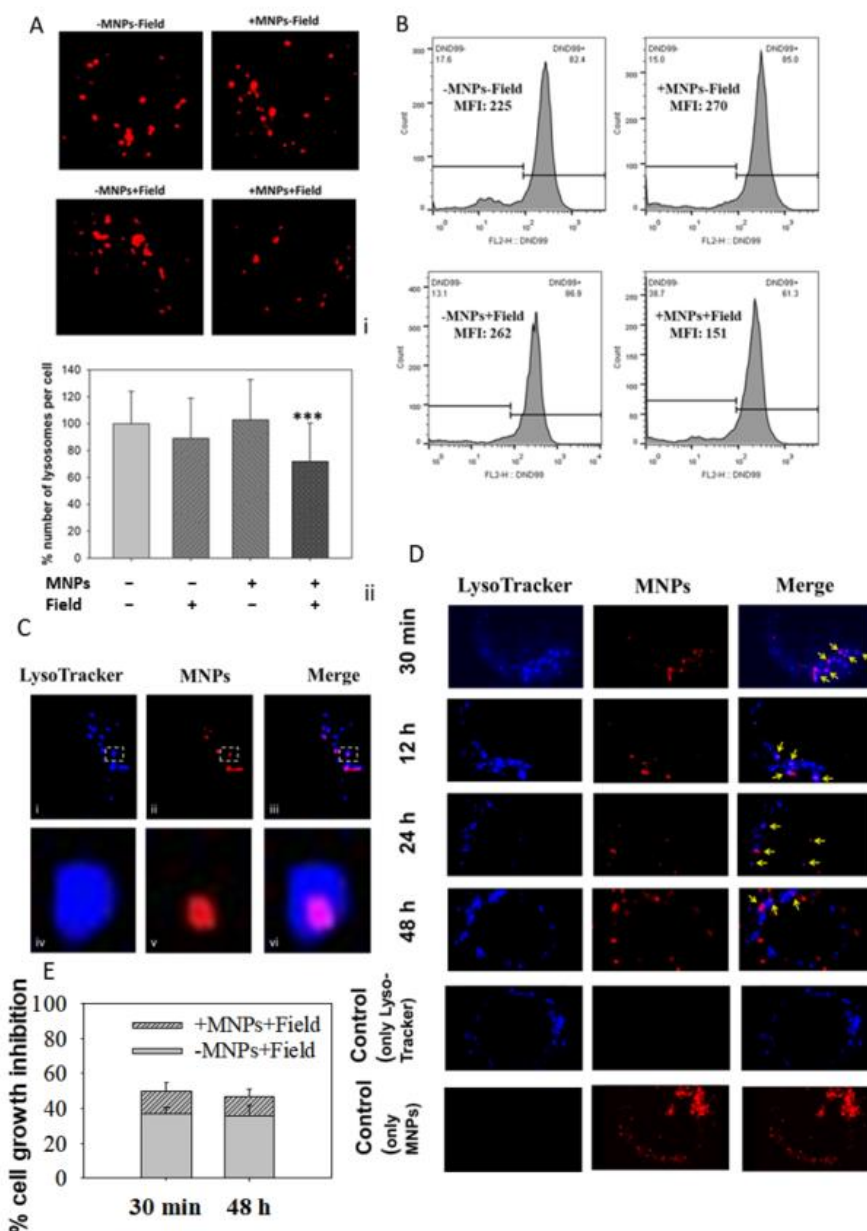


Figure 5. Effect of magnetomechanical stress on lysosomes. (A) Fluorescence microscopy of \pm MNPs \pm Field HT29 cells; lysosomes are stained red with the LysoTracker Red dye (i). (ii) Relative quantification of the number of lysosomes per cell expressed as % of the number counted in control ($-$ MNPs $-$ Field) cells. (B) Flow cytometry representative histograms of HT29 cells stained with LysoTracker Red. Median fluorescence intensity (MFI) values indicate the relative degree of LysoTracker fluorescence and, hence, the acidity level of lysosomes in various treatment groups. Fluorescence microscopy and flow cytometry analyses were conducted 2 h after magnetic field exposure. *** Asterisks indicate a statistically significant difference (Student's *t*-test, $p \leq 0.001$). (C) Co-localization of lysosomes stained with LysoTracker Blue and fluorescently labeled MNPs (red). (D) Time-dependent co-localization of lysosomes and MNPs. Fluorescence images were taken at various co-incubation time points of HT29 cells with MNPs. LysoTracker Blue dye was used to visualize the lysosomes, and fluorescently tagged MNPs (red) were used for the incubation (100 μ g/mL). Yellow arrays indicate co-localized MNPs and lysosomes. (E) Effect of MNPs co-incubation period on induced cell growth inhibition. HT29 cells were treated with MNPs (100 μ g/mL) for 30 min or 48 h and/or exposed to a static magnetic field of 200 mT. Cell growth was analyzed 48 h post magnetic field exposure with the SRB assay. Values represent the mean ($n = 3$) \pm S.D.

Interestingly, the highest co-localization rate of the MNPs with the lysosomes occurred after the shortest co-incubation period (30 min) (Figure 5D). Since fewer lysosomes were observed in +MNP+Field cells (Figure 5A), we proceeded to investigate whether the highest co-localization rate of the MNPs and the lysosomes correlates with enhanced growth inhibition. Thus, the cell growth inhibition induced by the magnetomechanical treatment was comparatively investigated between cells that were treated with the MNPs for either 30 min or 48 h. However, no significant difference was observed for either +MNP+Field (47% compared to a 50% inhibition rate for a 48 h or a 30 min co-incubation period, respectively) or –MNP+Field cells (36% compared to 37% inhibition rate for a 48 h or a 30 min co-incubation period, respectively) (Figure 5E).

3.5. Lysosomal Acidic Conditions Affect MNPs' Magnetic Properties

In order to investigate whether the exposure of MNPs to the lysosomal acidic environment affects their magnetic behavior, we examined the magnetic properties of the MNPs after being incubated in an acidic medium (pH 4.5) mimicking lysosomal condition. A $\approx 30\%$ drop in the M_s value was observed for the MNPs incubated for 24 h in acidic medium (pH 4.5, $M_s = 35.17 \pm 0.67$) compared to MNPs incubated in the neutral DIW (pH 7.0, $M_s = 50.74 \pm 2.6$) (Figure 6), as determined with the VSM method. Moreover, a 24 h incubation period in DIW did not seem to affect the magnetic properties of the MNPs as the M_s value measured was similar to the control (MNPs diluted in DIW and immediately rinsed and processed).

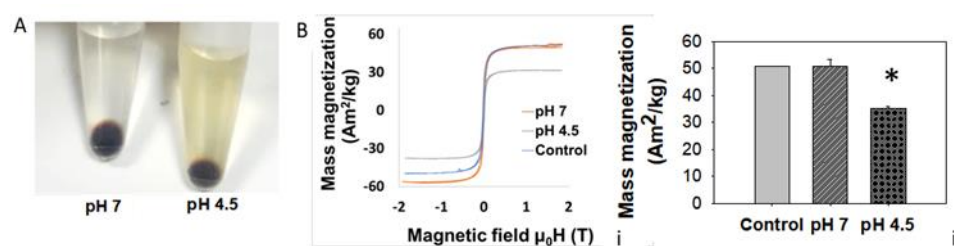


Figure 6. Magnetic properties of MNPs after incubation in acidic medium. (A) Photographic observation of MNPs, after an incubation period of 24 h at 37 °C in the neutral solution DIW (pH = 7) or acidic medium mimicking lysosomal environment (pH = 4.5). The pale yellow color in the acidic medium (pH = 4.5) indicates the degradation process. (B) pH-dependent magnetization measurements. (i) VSM (Vibrating sample magnetometry) results. (ii) Results presented as means \pm S.D. of three independent experiments. * Asterisk indicates a statistically significant difference compared to control (Student's *t*-test, $p \leq 0.05$).

4. Discussion

We previously comparatively examined the antiproliferative effects of spherical magnetite MNPs with a hydrodynamic diameter of 100 nm actuated by static or alternating low-frequency magnetic fields with varying intensity (40–200 mT), frequency (0–8 Hz), and field gradients in HT29 colon cancer cells. The highest cell growth inhibition observed (47% of control cell growth) was induced by the static field of the strongest field intensity (200 mT) and gradient [26]. Herein, we focused on the biological mechanisms mediating growth inhibition induced by the 200 mT static field in MNP-treated cancer cells.

First, we confirmed that the same growth inhibitory effect observed in HT29 cells is also applied in other colon cancer cell lines, specifically Caco-2 and CT26. Of note, while both human cell lines (HT29 and Caco-2) are well characterized and commonly used as in vitro colon cancer models, Caco-2 cells are regarded as a model of the small intestine, whereas HT29 cells as a model of the large intestine [31]. Moreover, these cell lines have different genetic and epigenetic alterations and different mutations in p53 [32]. HT29 and Caco-2 cell lines were derived from human patients while the CT26 cell line is of murine origin and was developed by exposing BALB/c mice to N-nitroso-N-methylur-ethane

(NMU), resulting in a rapidly growing grade IV carcinoma [33]. Thus, CT26 cells represent an advanced stage of carcinogenesis [34]. The cell growth inhibitory effects exerted by the combination of MNPs and the 200 mT static magnetic field applied in all of the above in vitro colon cancer models highlights the applicability and effectiveness of the biomedical applications that can be developed based on these findings. The applicability of our results is also illustrated by the fact that the relative orientation and geometry between the cells and the field did not seem to affect the exerted growth inhibitory effect.

Mechanotransduction, the conversion of mechanical stimuli to a biochemical response by the cell, plays a crucial role in cellular processes including proliferation [35,36]. Specifically, mechanical stress has been previously shown to inhibit the progression of the G2/M phase in vitro [37,38]. Cell cycle arrest in the G2/M phase has been proven to enhance the antitumor effects of known chemotherapeutic agents [39]. In fact, cancer cells have been shown to display cell-cycle-specific sensitivities for certain drugs [40]. This interplay between cell cycle phase and drug efficacy has significant implications for drug administration scheduling. Paclitaxel, for example, is an anticancer agent, used to treat different types of cancers including lung, breast, and ovarian cancer [41]. Paclitaxel, as a microtubule inhibitor, is more efficacious during mitosis. Many chemotherapeutic agents such as platinum-based compounds and cyclin-dependent kinases (CDKs) inhibitors that induce cell cycle arrest, have been shown to antagonistically interact with paclitaxel's activity in combination chemotherapy schemes, when given prior to or simultaneously with paclitaxel. On the same basis, various levels of synergy have been reported for many combinations of cell-cycle-specific drugs [42–44]. The sequence dependency of such interactions between antitumor drugs combined with agents that exert cell-cycle-specific activities may be considered so that synergistic effects can be achieved. Thus, there is a recently renewed interest in the discovery of novel CDK inhibitors, while pharmacologic inhibitors of CDKs 4 and 6 specifically have changed the treatment landscape for breast cancer [45–49]. In certain cases though, low therapeutic indexes, mixed cellular responses, and unexpected effects have been reported due to the diverse impact the inhibitors have in cells [42,48,50,51]. Therefore, the cytostatic effect exerted by the 200 mT static magnetic-field-actuated MNPs in HT29 cells is an important observation that could be further explored aiming at the development of novel anticancer combination therapies. Of note, it is a chemical-free approach that might have fewer implications when combined with other drugs. Furthermore, the p53 status of HT29 cells, which are p53-deficient [52], and the absence of dead cells in the +MNPs+Field-treated population indicate that a more thorough investigation of the observed effect should be conducted, focusing on different cell lines, both p53^{wt} and p53^{mut}.

Having observed a significant degree of co-localization between the internalized MNPs and the lysosomes, which is in line with the current literature [53,54], it was investigated whether the mechanical force applied by the internalized MNPs could affect organelles' integrity and, therefore, mediate LMP. Several formulations of non-targeted MNPs have been previously shown to preferentially accumulate in lysosomes [53,54]. Lysosomes are cytoplasmic organelles that contain membrane-enclosed degradative enzymes (hydrolases) and are responsible for the degradation of a variety of macromolecules. LMP, a process that leads to the release of the hydrolases from the lysosomal lumen to the cytosol, has been under investigation as a novel therapeutic strategy and proven effective in many cancer models [55]. Specifically, magnetomechanical disruption of the lysosomal membrane via the actuation of internalized MNPs has been successfully achieved in vitro [56–61]. The force generated here via the magnetic actuation of the internalized MNPs was calculated to reach ≈ 29 pN per cell. This value was calculated based on the specific MNP type used, field characteristics, and number of internalized nanoparticles under the mentioned experimental conditions [26] and lies within the force magnitude range where mechanotransduction occurs [62].

Interestingly, in +MNPs+Field cells, we observed a loss in the pH gradient evidenced both by the significantly lower MFI of the LysoTracker dye (151 au in +MNPs+Field cells compared to 225–270 au in the other treatment groups) and the small fraction of cells

exhibiting a LysoTracker positive status (63% in +MNPs+Field cells compared to 82–87% in the other treatment groups). Magnetomechanical disruption of the lysosomal membrane via the actuation of internalized MNPs has been achieved previously by other groups [56,57].

Remarkably, in our results, the degree of the +MNPs+Field-induced loss in the pH gradient, indicating a destabilized lysosomal/endosomal membrane, did not correlate with the degree of co-localization between MNPs and lysosomes. Crucially, the latter, along with the uptake rate of the MNPs by the cells, is time dependent.

We examined whether there are other parameters besides MNPs' and lysosomes' co-localization rate that affect the magnitude of the induced cell growth inhibition. Iron oxide nanoparticles, such as the MNPs used in this project, have been shown to be prone to degradation effects in acidic environments such as the interior of the lysosomes (pH 4.5–5.0) [63]. MNPs' degradation could affect their magnetic properties [64] and, thus, their ability to apply the magnetomechanical force partly responsible for the observed growth inhibition effects in +MNPs+Field cells.

Indeed, it was found that the acidic pH of the lysosomes affects the magnetic properties of the MNPs, an observation confirming previously published results [64]. The lack of correlation between the degree of MNPs' and lysosomes' co-localization and the degree of the loss of the pH gradient in +MNPs+Field cells is not completely clear, but could be attributed to magnetization loss.

5. Conclusions

Localized mechanical stress has been shown to significantly affect cancer cell proliferation and tumor growth dynamics; therefore, it is a very promising tool in cancer research. Magnetic nanoparticles allow for a highly localized and externally controlled application of mechanical stress. Herein, we further explored biological mechanisms involved in the growth inhibition induced in cancer cells by internalized MNPs actuated by a 200 mT static magnetic field. Of note, the stress applied did not induce cell death, but cell cycle arrest in the G2/M phase. Interestingly, as expected, the internalized MNPs were found to accumulate in the lysosomes while their structural integrity was affected post magnetic field exposure. It would be of particular interest to further study combinations of MNP-mediated lysosome-targeting strategies with chemotherapeutic agents to improve the anticancer activity of current anticancer treatments. We believe that future applications of our findings could lead to the development of novel anticancer combination treatment schemes incorporating MNPs, based on lysosome-targeting strategies enabled by these MNPs or the combination of the cytostatic magnetomechanical treatment proposed in this study with chemotherapeutic agents aiming at enhanced anticancer activity.

Author Contributions: Conceptualization, K.C., O.K. and K.S.; methodology, G.A., C.S. and K.S.; software, K.S., G.A. and C.S.; formal analysis, K.S., G.A. and C.S.; investigation, K.S. and G.A.; resources, K.C.; writing—original draft preparation, K.S.; writing—review and editing, K.C. and K.S.; supervision, K.C. and O.K.; funding acquisition, K.C. All authors have read and agreed to the published version of the manuscript.

Funding: This research received no external funding.

Institutional Review Board Statement: Not applicable.

Informed Consent Statement: Not applicable.

Data Availability Statement: Supporting data are available from the authors upon request.

Acknowledgments: Part of this study was conducted utilizing the facilities of the project “In-TechThrace: Integrated Technologies in biomedical research: multilevel biomarker analysis in Thrace” (MIS Code 5047285), under the Operational Program “Competitiveness, Entrepreneurship & Innovation” (EPAnEK), co-funded by the European Regional Development Fund (ERDF) and national resources (Partnership Agreement 2014–2020). The facilities of the project “OPENSREEN-GR: An Open-Access Research Infrastructure of Target-Based Screening Technologies and Chemical Biology for Human and Animal Health, Agriculture and Environment” (MIS 5002691), which is implemented

under the Action “Reinforcement of the Research and Innovation Infrastructure”, funded by the Operational Programme “Competitiveness, Entrepreneurship and Innovation” (NSRF 2014–2020) and co-financed by Greece and the European Union (European Regional Development Funds were also utilized).

Conflicts of Interest: The authors declare no conflict of interest.

References

- Goetzke, R.; Sechi, A.; De Laporte, L.; Neuss, S.; Wagner, W. Why the impact of mechanical stimuli on stem cells remains a challenge. *Cell. Mol. Life Sci.* **2018**, *75*, 3297–3312. [[CrossRef](#)]
- Urrutia, C.O.; Dominguez-García, M.V.; Flores-Estrada, J.; Laguna-Camacho, A.; Castillo-Cadena, J.; Flores-Merino, M.V. Mechanical Stimulation of Cells Through Scaffold Design for Tissue Engineering. *Scaffolds Tissue Eng. Mater. Technol. Clin. Appl.* **2017**, *147*, 9925. [[CrossRef](#)]
- Sun, J.; Chen, J.; Mohagheghian, E.; Wang, N. Force-induced gene up-regulation does not follow the weak power law but depends on H3K9 demethylation. *Sci. Adv.* **2020**, *6*, eaay9095. [[CrossRef](#)]
- Jain, R.K.; Martin, J.D.; Stylianopoulos, T. The Role of Mechanical Forces in Tumor Growth and Therapy. *Annu. Rev. Biomed. Eng.* **2014**, *16*, 321–346. [[CrossRef](#)]
- Cheng, G.; Tse, J.; Jain, R.K.; Munn, L.L. Micro-Environmental Mechanical Stress Controls Tumor Spheroid Size and Morphology by Suppressing Proliferation and Inducing Apoptosis in Cancer Cells. *PLoS ONE* **2009**, *4*, e4632. [[CrossRef](#)]
- Trepát, X. Viewpoint: Forcing Tumor Arrest. *Physics* **2011**, *4*, 85. [[CrossRef](#)]
- Montel, F.; Delarue, M.; Elgeti, J.; Malaquin, L.; Basan, M.; Risler, T.; Cabane, B. Stress Clamp Experiments on Multicellular Tumor Spheroids. *Phys. Rev. Lett.* **2011**, *107*, 188102. [[CrossRef](#)]
- Yu, H.; Mouw, J.K.; Weaver, V.M. Forcing form and function: Biomechanical regulation of tumor evolution. *Trends Cell Biol.* **2011**, *21*, 47–56. [[CrossRef](#)]
- Northcott, J.M.; Dean, I.S.; Mouw, J.K.; Weaver, V.M. Feeling stress: The mechanics of cancer progression and aggression. *Front. Cell Dev. Biol.* **2018**, *6*, 17. [[CrossRef](#)]
- Gahl, T.J.; Kunze, A. Force-Mediating Magnetic Nanoparticles to Engineer Neuronal Cell Function. *Front. Neurosci.* **2018**, *12*, 299. [[CrossRef](#)]
- Novoselova, I.P.; Neusch, A.; Brand, J.S.; Otten, M.; Safari, M.R.; Bartels, N.; Karg, M.; Farle, M.; Wiedwald, U.; Monzel, C. Magnetic nanoprobe for spatio-mechanical manipulation in single cells. *Nanomaterials* **2021**, *11*, 2267. [[CrossRef](#)]
- Zablotskii, V.; Lunov, O.; Dejneka, A.; Jastrabík, L.; Polyakova, T.; Syrovets, T.; Simmet, T. Nanomechanics of magnetically driven cellular endocytosis. *Appl. Phys. Lett.* **2011**, *99*, 183701. [[CrossRef](#)]
- Kauffmann, P.; Ith, A.; O’Brien, D.; Gaude, V.; Boué, F.; Combe, S.; Bruckert, F.; Schaack, B.; Dempsey, N.M.; Haguet, V.; et al. Diamagnetically trapped arrays of living cells above micromagnets. *Lab. Chip.* **2011**, *11*, 3153. [[CrossRef](#)]
- Zablotskii, V.; Syrovets, T.; Schmidt, Z.W.; Dejneka, A.; Simmet, T. Modulation of monocytic leukemia cell function and survival by high gradient magnetic fields and mathematical modeling studies. *Biomaterials* **2014**, *35*, 3164–3171. [[CrossRef](#)]
- Zhang, E.; Kircher, M.F.; Koch, M.; Eliasson, L.; Goldberg, S.N.; Renström, E. Dynamic magnetic fields remote-control apoptosis via nanoparticle rotation. *ACS Nano* **2014**, *8*, 3192–3201. [[CrossRef](#)]
- Orr, A.W.; Helmke, B.P.; Blackman, B.R.; Schwartz, M.A. Mechanisms of Mechanotransduction. *Dev. Cell* **2006**, *10*, 11–20. [[CrossRef](#)]
- Leulmi, S.; Chauchet, X.; Morcrette, M.; Ortiz, G.; Joisten, H.; Sabon, P.; Livache, T.; Hou, Y.; Carrière, M.; Lequien, S.; et al. Triggering the apoptosis of targeted human renal cancer cells by the vibration of anisotropic magnetic particles attached to the cell membrane. *Nanoscale* **2015**, *7*, 15904–15914. [[CrossRef](#)]
- Cheng, Y.; Muroski, M.E.; Petit, D.C.M.C.; Mansell, R.; Vemulkar, T.; Morshed, R.A.; Han, Y.; Balyasnikova, I.V.; Horbinski, C.M.; Huang, X.; et al. Rotating magnetic field induced oscillation of magnetic particles for in vivo mechanical destruction of malignant glioma. *J. Control. Release* **2016**, *223*, 75–84. [[CrossRef](#)]
- Butcher, D.T.; Alliston, T.; Weaver, V.M. A tense situation: Forcing tumour progression. *Nat. Rev. Cancer* **2009**, *9*, 108–122. [[CrossRef](#)]
- Naud, C.; Thébault, C.; Carrière, M.; Hou, Y.; Morel, R.; Berger, F.; Diény, B.; Joisten, H. Cancer treatment by magneto-mechanical effect of particles, a review. *Nanoscale Adv.* **2020**, *2*, 3632–3655. [[CrossRef](#)]
- Kim, D.H.; Rozhkova, E.A.; Ulasov, I.V.; Bader, S.D.; Rajh, T.; Lesniak, M.S.; Novosad, V. Biofunctionalized magnetic-vortex microdiscs for targeted cancer-cell destruction. *Nat. Mater.* **2010**, *9*, 165–171. [[CrossRef](#)]
- Shen, Y.; Wu, C.; Uyeda, T.Q.P.; Plaza, G.R.; Liu, B.; Han, Y.; Lesniak, M.S.; Cheng, Y. Elongated nanoparticle aggregates in cancer cells for mechanical destruction with low frequency rotating magnetic field. *Theranostics* **2017**, *7*, 1735–1748. [[CrossRef](#)]
- Chen, M.; Wu, J.; Ning, P.; Wang, J.; Ma, Z.; Huang, L.; Plaza, G.R.; Shen, Y.; Xu, C.; Han, Y.; et al. Remote Control of Mechanical Forces via Mitochondrial-Targeted Magnetic Nanospinners for Efficient Cancer Treatment. *Small* **2020**, *16*, e1905424. [[CrossRef](#)]
- Martínez-Banderas, A.I.; Aires, A.; Teran, F.J.; Perez, J.E.; Cadenas, J.F.; Alsharif, N.; Ravasi, T.; Cortajarena, A.L.; Kosel, J. Functionalized magnetic nanowires for chemical and magneto-mechanical induction of cancer cell death. *Sci. Rep.* **2016**, *6*, 35786. [[CrossRef](#)]

25. Wong, D.W.; Gan, W.L.; Liu, N.; Lew, W.S. Magneto-Actuated cell apoptosis by biaxial pulsed magnetic field. *Sci. Rep.* **2017**, *7*, 10919. [[CrossRef](#)]
26. Spyridopoulou, K.; Makridis, A.; Maniotis, N.; Karypidou, N.; Myrovali, E.; Samaras, T.; Angelakeris, M.; Chlichlia, K.; Kalogirou, O. Effect of low frequency magnetic fields on the growth of MNP-treated HT29 colon cancer cells. *Nanotechnology* **2018**, *29*, 175101. [[CrossRef](#)]
27. Maniotis, N.; Makridis, A.; Myrovali, E.; Theopoulos, A.; Samaras, T.; Angelakeris, M. Magneto-mechanical action of multimodal field configurations on magnetic nanoparticle environments. *J. Magn. Magn. Mater.* **2017**, *470*, 6–11. [[CrossRef](#)]
28. Vichai, V.; Kirtikara, K. Sulforhodamine B colorimetric assay for cytotoxicity screening. *Nat. Protoc.* **2006**, *1*, 1112–1116. [[CrossRef](#)]
29. Spyridopoulou, K.; Aindelis, G.; Lampri, E.; Giorgalli, M.; Lamprianidou, E.; Kotsianidis, I.; Tsingotjidou, A.; Pappa, A.; Kalogirou, O.; Chlichlia, K. Improving the Subcutaneous Mouse Tumor Model by Effective Manipulation of Magnetic Nanoparticles-Treated Implanted Cancer Cells. *Ann. Biomed. Eng.* **2018**, *46*, 1975–1987. [[CrossRef](#)]
30. Foty, R. A simple hanging drop cell culture protocol for generation of 3D spheroids. *J. Vis. Exp.* **2011**, *20*, 4–7. [[CrossRef](#)]
31. Grajek, W.; Olejnik, A. Epithelial cell cultures in vitro as a model to study functional properties of food. *Pol. J. Food Nutr. Sci.* **2004**, *13*, 5–24.
32. Ahmed, D.; Eide, P.W.; Eilertsen, I.A.; Danielsen, S.A.; Eknæs, M.; Hektoen, M.; Lind, G.E.; Lothe, R.A. Epigenetic and genetic features of 24 colon cancer cell lines. *Oncogenesis* **2013**, *2*, e71. [[CrossRef](#)]
33. Castle, J.C.; Loewer, M.; Boegel, S.; de Graaf, J.; Bender, C.; Tadmor, A.D.; Boisguerin, V.; Bukur, T.; Sorn, P.; Paret, C.; et al. Immunomic, genomic and transcriptomic characterization of CT26 colorectal carcinoma. *BMC Genom.* **2014**, *15*, 190. [[CrossRef](#)]
34. Forn, M.; Díez-Villanueva, A.; Merlos-Suárez, A.; Muñoz, M.; Lois, S.; Carriò, E.; Jordà, M.; Bigas, A.; Batlle, E.; Peinado, M.A. Overlapping DNA methylation dynamics in mouse intestinal cell differentiation and early stages of malignant progression. *PLoS ONE* **2015**, *10*, e0123263. [[CrossRef](#)]
35. Uray, I.P.; Uray, K. Mechanotransduction at the Plasma Membrane-Cytoskeleton Interface. *Int. J. Mol. Sci.* **2021**, *22*, 11566. [[CrossRef](#)]
36. Wu, C.; Shen, Y.; Chen, M.; Wang, K.; Li, Y.; Cheng, Y. Recent Advances in Magnetic-Nanomaterial-Based Mechanotransduction for Cell Fate Regulation. *Adv. Mater.* **2018**, *30*, e1705673. [[CrossRef](#)]
37. Paul, N.E.; Denecke, B.; Kim, B.; Dreser, A.; Bernhagen, J.; Pallua, N. The effect of mechanical stress on the proliferation, adipogenic differentiation and gene expression of human adipose-derived stem cells. *J. Tissue Eng. Regen. Med.* **2018**, *12*, 276–284. [[CrossRef](#)]
38. Damm, T.B.; Franco-Obregón, M.; Egli, M. Gravitational force modulates G2/M phase exit in mechanically unloaded myoblasts. *Cell Cycle* **2013**, *12*, 3001–3012. [[CrossRef](#)]
39. DiPaola, R.S. To arrest or not to G(2)-M Cell-cycle arrest: Commentary re: A. K. Tyagi et al., Silibinin strongly synergizes human prostate carcinoma DU145 cells to doxorubicin-induced growth inhibition, G(2)-M arrest, and apoptosis. *Clin. Cancer Res.* **2002**, *8*, 3311–3314. [[PubMed](#)]
40. Lieftink, C.; Beijersbergen, R.L. It takes two to tango, and the right music: Synergistic drug combinations with cell-cycle phase-dependent sensitivities. *EBioMedicine* **2021**, *69*, 103448. [[CrossRef](#)]
41. Stage, T.B.; Bergmann, T.K.; Kroetz, D.L. Clinical pharmacokinetics of paclitaxel monotherapy: An updated literature review. *Clin. Pharmacokinet.* **2018**, *57*, 7. [[CrossRef](#)] [[PubMed](#)]
42. Johnson, T.I.; Minter, C.J.; Kottmann, D.; Dunlop, C.R.; Fernández, S.B. de Q.; Carnevalli, L.S.; Wallez, Y.; Lau, A.; Richards, F.M.; Jodrell, D.I. Quantifying cell cycle-dependent drug sensitivities in cancer using a high throughput synchronisation and screening approach. *EBioMedicine* **2021**, *68*, 103396. [[CrossRef](#)]
43. Xiong, X.; Sui, M.; Fan, W.; Kraft, A.S. Cell cycle dependent antagonistic interactions between paclitaxel and carboplatin in combination therapy. *Cancer Biol. Ther.* **2007**, *6*, 1067–1073. [[CrossRef](#)]
44. Jin, D.; Tran, N.; Thomas, N.; Tran, D.D. Combining CDK4/6 inhibitors ribociclib and palbociclib with cytotoxic agents does not enhance cytotoxicity. *PLoS ONE* **2019**, *14*, e0223555. [[CrossRef](#)]
45. Wang, X.; Deng, K.; Wang, C.; Li, Y.; Wang, T.; Huang, Z.; Ma, Y.; Sun, P.; Shi, Y.; Yang, S.; et al. Novel CDKs inhibitors for the treatment of solid tumour by simultaneously regulating the cell cycle and transcription control. *J. Enzym. Inhib. Med. Chem.* **2020**, *35*, 414–423. [[CrossRef](#)]
46. Zheng, L.; Yang, Y.; Bao, J.; He, L.; Qi, Y.; Zhang, J.Z.H. Discovery of novel inhibitors of CDK2 using docking and physics-based binding free energy calculation. *Chem. Biol. Drug Des.* **2022**, *99*, 662–673. [[CrossRef](#)]
47. Jing, L.; Tang, Y.; Xiao, Z. Discovery of novel CDK inhibitors via scaffold hopping from CAN508. *Bioorg. Med. Chem. Lett.* **2018**, *28*, 1386–1391. [[CrossRef](#)]
48. Goel, S.; DeCristo, M.J.; McAllister, S.S.; Zhao, J.J. CDK4/6 inhibition in cancer: Beyond cell cycle arrest. *Trends Cell Biol.* **2018**, *28*, 911. [[CrossRef](#)]
49. Juaid, N.; Amin, A.; Abdalla, A.; Reese, K.; Alamri, Z.; Moulay, M.; Abdu, S.; Miled, N. Anti-Hepatocellular Carcinoma Biomolecules: Molecular Targets Insights. *Int. J. Mol. Sci.* **2021**, *22*, 10774. [[CrossRef](#)] [[PubMed](#)]
50. Suski, J.M.; Braun, M.; Strmiska, V.; Sicsinski, P. Targeting cell-cycle machinery in cancer. *Cancer Cell* **2021**, *39*, 759–778. [[CrossRef](#)]
51. Sherr, C.J.; Bartek, J. Cell Cycle-Targeted Cancer Therapies. *Annu. Rev. Cancer Biol.* **2017**, *1*, 41–57. [[CrossRef](#)]
52. Tao, Y.; Zhang, P.; Girdler, F.; Frascogna, V.; Castedo, M.; Bourhis, J.; Kroemer, G.; Deutsch, E. Enhancement of radiation response in p53-deficient cancer cells by the Aurora-B kinase inhibitor AZD1152. *Oncogene* **2008**, *27*, 3244–3255. [[CrossRef](#)] [[PubMed](#)]

53. Master, A.M.; Williams, P.N.; Pothayee, N.; Zhang, R.; Vishwasrao, H.M.; Golovin, Y.I.; Riffle, J.S.; Sokolsky-Papkov, M.; Kabanov, A.V. Summary for Policymakers. In *Climate Change 2013—The Physical Science Basis*; Intergovernmental Panel on Climate Change: Geneva, Switzerland; Cambridge University Press: Cambridge, UK, 2015; Volume 1, pp. 1–30. ISBN 9788578110796.
54. Shen, H.; Tong, S.; Bao, G.; Wang, B. Structural responses of cells to intracellular magnetic force induced by superparamagnetic iron oxide nanoparticles. *Phys. Chem. Chem. Phys.* **2014**, *16*, 1914–1920. [[CrossRef](#)]
55. Boya, P.; Kroemer, G. Lysosomal membrane permeabilization in cell death. *Oncogene* **2008**, *27*, 6434–6451. [[CrossRef](#)]
56. Domenech, M.; Marrero-Berrios, I.; Torres-Lugo, M.; Rinaldi, C. Lysosomal Membrane Permeabilization by Targeted Magnetic Nanoparticles in Alternating Magnetic Fields. *ACS Nano*. **2013**, *7*, 5091–5101. [[CrossRef](#)]
57. Connord, V.; Clerc, P.; Hallali, N.; El Hajj Diab, D.; Fourmy, D.; Gigoux, V.; Carrey, J. Real-Time Analysis of Magnetic Hyperthermia Experiments on Living Cells under a Confocal Microscope. *Small* **2015**, *11*, 2437–2445. [[CrossRef](#)]
58. Lunov, O.; Uzhytchak, M.; Smolková, B.; Lunova, M.; Jirsa, M.; Dempsey, N.M.; Dias, A.L.; Bonfim, M.; Hof, M.; Jurkiewicz, P.; et al. Remote Actuation of Apoptosis in Liver Cancer Cells via Magneto-Mechanical Modulation of Iron Oxide Nanoparticles. *Cancers* **2019**, *11*, 1873. [[CrossRef](#)]
59. Xiang, Y.; Li, N.; Liu, M.; Chen, Q.; Long, X.; Yang, Y.; Xiao, Z.; Huang, J.; Wang, X.; Yang, Y.; et al. Nanodrugs Detonate Lysosome Bombs. *Front. Pharmacol.* **2022**, *13*, 909504. [[CrossRef](#)] [[PubMed](#)]
60. Tsiapla, A.; Uzunova, V.; Oreshkova, T.; Angelakeris, M. Cell Behavioral Changes after the Application of Magneto-Mechanical Activation to Normal and Cancer Cells. *Magnetochemistry* **2022**, *8*, 21. [[CrossRef](#)]
61. Lopez, S.; Hallali, N.; Lalatonne, Y.; Hillion, A.; Antunes, J.C.; Serhan, N.; Clerc, P.; Fourmy, D.; Motte, L.; Carrey, J.; et al. Magneto-mechanical destruction of cancer-associated fibroblasts using ultra-small iron oxide nanoparticles and low frequency rotating magnetic fields. *Nanoscale Adv.* **2022**, *4*, 421–436. [[CrossRef](#)]
62. Cost, A.L.; Ringer, P.; Chrostek-Grashoff, A.; Grashoff, C. How to Measure Molecular Forces in Cells: A Guide to Evaluating Genetically-Encoded FRET-Based Tension Sensors. *Cell. Mol. Bioeng.* **2015**, *8*, 96. [[CrossRef](#)]
63. Gutiérrez, L.; Romero, S.; da Silva, G.B.; Costo, R.; Vargas, M.D.; Ronconi, C.M.; Serna, C.J.; Veintemillas-Verdaguer, S.; del Puerto Morales, M. Degradation of magnetic nanoparticles mimicking lysosomal conditions followed by AC susceptibility. *Biomed. Eng. Biomed. Tech.* **2015**, *60*, 417–425. [[CrossRef](#)] [[PubMed](#)]
64. Mazuel, F.; Espinosa, A.; Luciani, N.; Reffay, M.; Le Borgne, R.; Motte, L.; Desboeufs, K.; Michel, A.; Pellegrino, T.; Lalatonne, Y.; et al. Massive Intracellular Biodegradation of Iron Oxide Nanoparticles Evidenced Magnetically at Single-Endosome and Tissue Levels. *ACS Nano*. **2016**, *10*, 7627–7638. [[CrossRef](#)] [[PubMed](#)]